First-Principles Simulations for $CuInGaSe_2$ (CIGS) Solar Cells

2

Yu-Wen Cheng, Hong-Tao Xue, Fu-Ling Tang, and Jingbo Louise Liu

Contents

Author Contribution

Y.-W. Cheng did the DOS calculation on the CIS, while H.-T. Xue did the DOS on the CGS system. F.-L. Tang extended the LDOS and generated some of the figures and supervised the calculations, and J. L. Liu edited the manuscript and assisted with the PBE analyses.

Cheng summarized this chapter from the results of Tang's group, and Xue took part in all the works. The authors further acknowledge that there is no financial relationship with the editors or publisher and have contributed original work in this chapter, other than what acknowledged or appropriately cited with copyright permission.

Y.-W. Cheng · H.-T. Xue
Department of Materials Science and Engineering, Lanzhou University of Technology, Lanzhou, China
e-mail: 1109551346@qq.com; xueht987@163.com

F.-L. Tang (✉)
Department of Materials Science and Engineering, Lanzhou University of Technology, Lanzhou, China

Department of Chemistry, Texas A&M University, Kingsville, TX, USA
e-mail: tfl@lut.cn

J. L. Liu
Department of Chemistry, Texas A&M University-Kingsville, Kingsville, TX, USA

Department of Chemistry, Texas A&M University (TAMU), College Station, TX, USA
e-mail: Jingbo.Liu@tamuk.edu

T. A. Atesin et al. (eds.), *Nanostructured Materials for Next-Generation Energy Storage and Conversion*, https://doi.org/10.1007/978-3-662-59594-7_2

Abstract

In this chapter, simulations for $CuInGaSe_2$ (CIGS) solar cell materials are illustrated from the viewpoint of first-principles calculations. The solar cell materials under high pressure, upon doping, the atomistic distribution in solar cell materials, and the interface in solar cells were studied. Their lattice structure and mechanics, optical, and electrical properties were studied. Our purpose is to obtain quantitative atomic and electronic structure information in the battery material, and then to understand the relationship among composition, structure, and performance. This will help to design element composition and to determine the technical process parameters. Our study may provide theoretical guidance and help to reduce the usage of highly toxic and scarce elements, reduce battery manufacturing costs, and mitigate potential environmental pollution. In addition, interface states in $CuInGaSe_2$ thin-film solar cell always do harm to its overall performance by reducing both open-circuit voltage and photoelectric conversion efficiency. In order to maximally weaken the negative impacts of interface states, we used the first-principles calculation to systematically study the local structures and electronic properties of the interfaces. The aim of these simulations was to deeply understand the relationship among the local structures of the interfaces, interface states, and $CuInGaSe_2$ thin-film solar cell performances, and to reveal the micro-mechanism of photoelectric changes introduced by interface states. As theoretical guides, quantitative results at atomic scale will be helpful to design the chemical components of the cell's materials and those at the interfaces, to modify the interface structures, to manipulate the interface properties, to take advantage of so-called interface engineering, and then to improve the cell's performances.

2.1 Introduction

Simulations are powerful tools for researching on solar cell materials, which are important compensation for experimental research. Homogeneous and single-phase $CuInGaSe_2$ (CIGS) films are considered to be suitable for materials for high-efficiency CIGS-based solar cells. But as has been found in many previous investigations, the existence of the phase separation of phase (Copper, Cu; Indium, In; Gallium, Ga; and Sulfur, S) $CuInGaS_2$ (CIS) and CGS (or In-rich CIGS and Ga-rich CIGS) in CIGS alloys resulting in the inhomogeneous distribution of elemental Ga. Ludwig et al. found that CIGS alloys tend to phase-separating into In-rich and Ga-rich CIGS phases in thermal equilibrium below the room temperature [23]. Tinoco et al. obtained the T(x) phase diagram of $CuIn_{1-x}Ga_xSe2$ (Selenium, Se) alloys at a temperature above 1073 K by using x-ray diffraction and differential thermal analysis [34]. Yan et al. [47] observed the alloy inhomogeneity associated

with the spatial fluctuation in In and Ga concentrations in CIGS films [47]. Huang et al. have calculated the phase diagram (the binodal curve) of CIGS as a function of Ga concentration and have separately found that the critical temperature (Tc) in CIGS is 420 K [14]. All of these theoretical studies showed that CIGS has a tendency to phase separating at low temperature. The existence of phase-separation of $CuInSe_2$ (or Se-rich CISS) and $CuInS_2$ (or S-rich CISS) in CISS alloys resulting in the inhomogeneous distribution of Se-S atoms. Engelmann et al. have produced graded CISS alloy films by reacting CuInSe2 films in a flowing hydrogen sulfide/argon (H_2S/Ar) atmosphere [10]. Sheppard et al. have found that it is a typical reaction that the two distinct and stable ternary phases $CuInSe_2$ and $CuInS_2$ form in CISS alloys during the selenization and sulfurization of CuIn metallic alloys [30]. A direct consequence of the inhomogeneous distribution of Se-S atoms is that the band gap of the CISS absorber films is not uniform. The performances of devices produced from these phase-separation absorber films are inferior, such as causing to having open-circuit voltages and fill factors due to the limited band gap value of absorber films [29, 31]. Werner et al. have shown that even small fluctuations in the composition is un-favored [39], due to the phase separation, which can affect the electronic and optical properties of CIGS. It has been proved that $Cu(In_{1-x}Ga_x)Se_2$ (CIGS) alloys have the phase-separation behavior [18, 34] and inhomogeneity [3]. Recent first-principles study of phase equilibrium of similar pseudobinary alloys, $CuInSe_2$-$CuGaSe_2$ [41, 45] and $CuInSe_2$-$CuAlSe_2$ [32, 40], (Aluminum, Al), has predicted the miscibility gap and upper critical solution temperature (UCST) or consolute temperature of these alloys [33, 46], though the available phase diagrams show complete miscibility in the solid state [19, 23]. All of these literatures mean that the knowledge of the alloy phase equilibrium and homogeneity is essential for effective designing of the CISS alloy.

The photoelectric properties of CIGS cells depend not only on the composition and properties of the materials each layer but also on the composition, the structure, and the properties of the interface between the adjacent layers; this is because of the abrupt change of structure at the interface between adjacent layers will lead to the appearance of the interface states and change the band structure of the semiconductor and will have a serious negative impact on the battery performance. Therefore, it is important to study the structure of the interface and eliminate the interface states. Sandino et al. used high-resolution transmission electron microscopy (HRTEM) to analyze the cross-sectional of Mo/CIS interface (Molybdenum, Mo), and observed the formation of a very thin MoS_2 layer (∼15–25 nm) among the Mo/CIS interface [28]. Tomić et al. used a hybrid density functional theory to study the electronic structure of the wurtzite $CuInS_2$ material [36]. Dong et al. studied the band alignment at the interface of cadenium sulfide/zinc oxide (CdS/ZnO) heterojunction and suggested that the interface of CdS/ZnO possesses type-II alignment [9]. Derkaouietal et al. studied ZnO/CdS/CdTe (cadmium telluride, CdTe) multilayer coatings' optical characteristics by using first-principles calculations and found that ZnO(300 nm)/CdS(10 nm)/CdTe (1000 nm) configuration solar absorption efficiency was larger than 80% in the visible region [8]. Hong et al. studied bond characteristics and interfacial energetic and electronic structure of $Mo/MoSi_2$ (001) interface by the first-principles calculation [12]. Liu et al. deposited a ZnO

intermediate layer on the Cu_2ZnSnS_4 (CZTS) (Tin, Sn) absorber and Mo back contact interface [21]. Yang et al. used X-ray photoelectron spectroscopy (XPS) combined with first-principles calculations to study the band alignments of the CZTS/ZnO heterojunction and suggested that ZnO can be an attractive Cd-free buffer layers candidate for CZTS-based solar cells [48]. Bao et al. studied the valence band offsets in the CZTS/ZnO heterointerface by calculating the local density of states of each atom in the supercell and found that the CZTS/ZnO interface is of type I heterojunction [1]. For passivation interface states, fluorine (F), hydrogen (H), and chlorine (Cl) are the common passivation elements for they easily get electrons from other elements when they formed compound, and researchers have studied F and H [20] and Cl [38] passivation for silicon carbide/silica oxide (SiC/SiO_2) and gafnium dioxide/gallium arsenide (HfO_2/GaAs) interfaces, respectively, by the first-principles calculations. These results showed that the interface states can be reduced by F, H, and Cl atoms.

In this chapter, we illustrate the first-principles simulations on solar cell materials. Their lattice structures and electronic and photonic properties are provided. We study their lattice structure and mechanics, optical, and electrical properties. Our purpose is to obtain quantitative atomic and electronic structure information in about the battery material, and then to understand the relationship among the composition, the structure, and the performances.

2.2 Methods

2.2.1 First-Principles Calculation and the Software VASP

In this chapter, most of the calculation works were carried out within the Vienna ab initio simulation package (VASP) [15, 16] based on first-principles density functional theory (DFT) with the Perdew-Burke-Ernzerhof (PBE) version [25] of the generalized gradient approximation (GGA). The projector augmented wave (PAW) method [17] was applied to describe the pseudopotential. The electronic configurations are [Ar] $3d^{10}4s^1$, [Kr] $5s^25p^1$, [Ar] $4s^24p^1$, [Ar] $4s^24p^4$, [Ar] $3d^{10}4s^2$, [Kr] $4d^{10}5s^25p^2$, [Kr] $3d^{10}5s^2$, [Ne] $3s^23p^1$, [Ne] $3s^23p^4$, $2s^22p^4$, $1s^1$ for copper, indium, gallium, selenium, zinc, tin, cadmium, aluminum, sulfur, oxygen, hydrogen, respectively. The conjugate gradient (CG) [50] method was used to optimize the lattice structure. The tetrahedron method with Bloch corrections [2] was used for calculating the interface binding energy, the band structure, and the density of states (DOS) in all systems. Meanwhile, our theoretical approach is based on the GGA with on-site Coulomb interaction parameter (GGA + U method) (taking account of the Hubbard correction) [13].

2.2.2 Cluster Expansion and Monte Carlo (MC) Simulations

As the Monto Carlo (MC) simulation of an $A_{1-x}B_x$ binary alloy involves comparing the energy of many different atomic configurations, it requires calculation of the total

energy for each of these configurations of placing atoms A and B on n sites of the underlying Bravais lattice. But in fact, it would be infeasible to calculate the total energy of all these configurations from first principles because the number of these configurations 2^n becomes enormous even for a modest number of sites n. Therefore, in this work we first employed the cluster expansion (CE) method, which is a well-established method and has been extensively and successfully used in many alloys [27, 37, 42–44], to obtain the effective cluster interactions (ECIs) that define a computationally efficient Hamiltonian for the configurational energy of an alloy. And then the ECIs were used as the main input parameters to performing MC simulations. The CE enables prediction of the energy of any configuration from the energies of a small number of configurations (typically between 30 and 50), thus making the procedure amenable to using of first-principles calculations [37].

In an $A_{1-x}B_x$ binary alloy, the CE is defined by first specifying occupation variables s_i to each of the n atomic sites ($i = 1, 2, 3 \ldots n$). The occupation variables s_i take the value +1 or −1 depending on the A atom or the B atom occupying the site. Each of the arrangements of these occupation variables on the atomic sites is called a configuration and is represented by a vector $\boldsymbol{s}$ which contains the value of the occupation variable for each atomic site in the $A_{1-x}B_x$ binary alloy. This approach is known as the structure inversion method (SIM) or the Collony-Williams method [7]. Once the cluster expansion has been constructed, i.e., the ECIs have been obtained, the energy of any configuration can be calculated by using Eq. 2.1 at a very small computational cost. Therefore, the aim of the CE method is to determine a limited set of ECIs such that the expansion can be truncated and computational expense is minimized while the predictive power is maximized.

2.3 Simulation Results

2.3.1 Solar Cell Materials under High Pressure and Phase Transformation

2.3.1.1 Phase Diagram of $CuGaSe_2$

The total energy of per $CuGaSe_2$ unit, lattice constants, bulk modulus, and pressure derivative of the bulk modulus for the three phases under zero-pressure were obtained by fitting the *Energy-Volume (E-V)* data points to the Murnaghan equation of state (EOS) [24]. The calculated total energy of per $CuGaSe_2$ unit as a function of volume for three structures are shown in Fig. 2.1. From these *Energy-Volume* (*E-V*) curves, it is clear find that the zero-pressure equilibrium structure of the $I\bar{4}2d$ phase has the lowest energy, which is the most stable structure. As the pressure increasing, the lattice volume decreases: the $Fm\bar{3}m$ structure and then *Cmcm* structure has the lowest energy sequentially. The inset of Fig. 2.1 shows the variation of the Gibbs free energy (*G*, kJ/mol) of the three phases as a function of pressure (*P*, Pa). The *G-P* curves can predict the possibility of the pressure-induced transformations between the three phases as well as the stability of the three phases under high pressure. As can be seen in Figure 2.1, when the pressure is below 11.87 GPa, the $I\bar{4}2d$ phase has a lower Gibbs free energy than that of the $Fm\bar{3}m$ phase, which indicates that the $I\bar{4}2d$

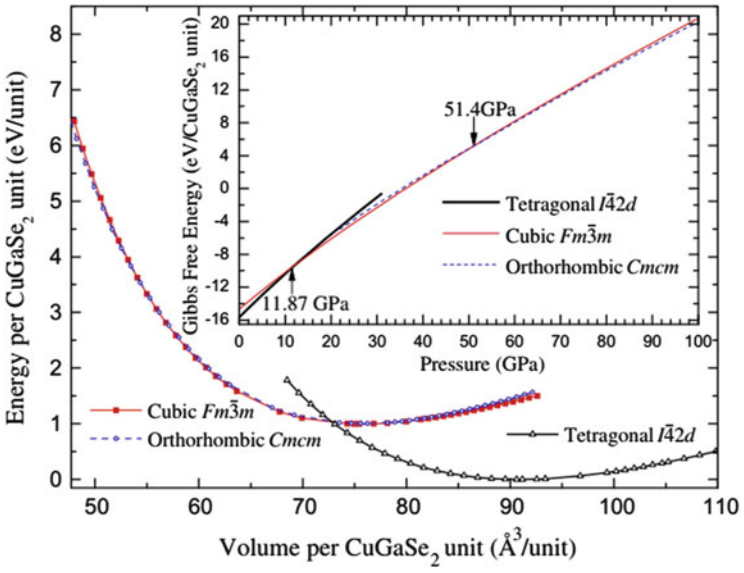

Fig. 2.1 Energy-volume curves and Gibbs free energy (inset) of CGS phase transition. The energy of I42d phase at zero pressure is set as 0 eV

phase is thermodynamically more stable than that of the $Fm\bar{3}m$ phase below 11.87 GPa, vice versa. Therefore, the point of intersections of curves corresponding to two phases gives us the pressure and the Gibbs free energy (at 0 K) for the phase transformation. Such a CGS $I\bar{4}2d$ to $Fm\bar{3}m$ phase transition pressure 11.87 GPa from *G-P* curves is in good agreement with the previous experimental result (13 GPa). For the *Cmcm* phase, at pressures above 51.4 GPa, it is thermodynamically more stable than the $Fm\bar{3}m$ phase due to its lower Gibbs free energy. While below this pressure, it is less stable than the latter one. Hence, our calculations indicate that it is possible for CGS ($CuGaSe_2$) to transform from the cubic $Fm\bar{3}m$structure to an orthorhombic *Cmcm* structure at about 51 GPa. The results imply that the structure of CGS is more harder than that of CIS (CuInGaS2).

Figure 2.2 shows the volume versus the pressure relation. This relation provides the information on about the volume decrease (per $CuGaSe_2$ unit), $-\Delta V/V_0$, at each phase transitions. It can be found that the volume decrease at the $I\bar{4}2d$ to $Fm\bar{3}m$ transition is 13.3%. And the calculated lattice parameter of the $Fm\bar{3}m$ structure at 16.21 GPa is $a = 5.057(5)$ Å. The corresponding volume decrease at the $Fm\bar{3}m$ to *Cmcm* transition is 0.49%. The calculated unit cell of the orthorhombic *Cmcm* structure at 54.91 GPa is $a = 4.726(3)$ Å, $b = 4.869(7)$ Å, and $c = 4.644(4)$ Å. The atomic position of the *Cmcm* structure (0, *y*, 1/4) at this pressure with *y* (Cu/Ga) = 0.690(6) and *y*(Se) = 0.195(2) is obtained. The transition pressures and the volume reductions are summarized and compared with the experimental data as shown in Fig. 2.3. It is readily seen that the calculations give a good description of the experimental result [35]. It should be noted that the calculations' results are obtained at 0 K, while the experimental results were always obtained at

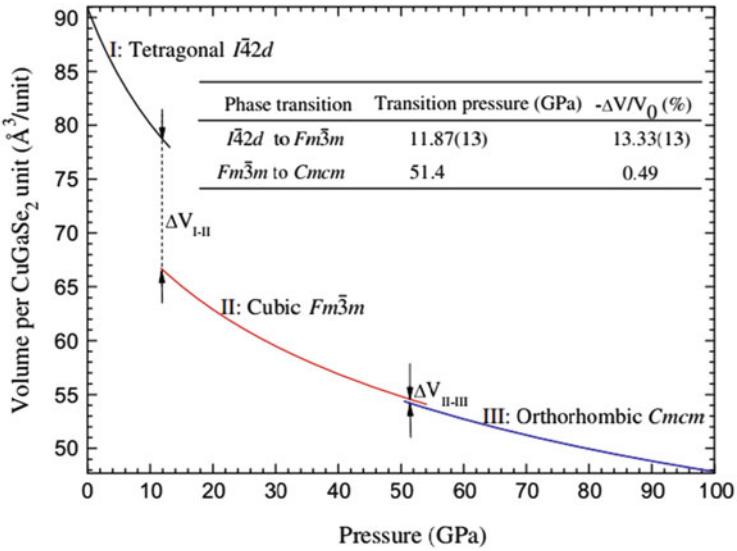

Fig. 2.2 Volume-pressure curves of CGS phase transition upon pressure between 0 and 100 GPa. The internal table shows the transition pressure and volume reduction. The internal table shows the transition pressure and the volume reduction, compared with the existing experimental data [35] in parentheses

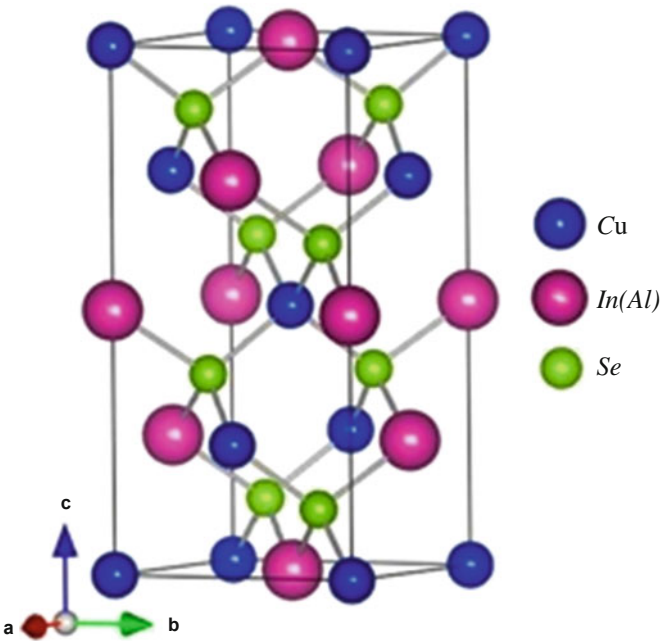

Fig. 2.3 Simulated unit cell diagram for the chalcopyrite system $CuIn_{1-x}Al_xSe_2$

ambient temperature. The possible inaccuracy of total-energy calculation results is amplified of the computation of the transition pressures. For example, in case of the phase transition of $I\bar{4}2d$ to $Fm\bar{3}m$, an error of 0.1 eV in the total-energy computation would lead to an error of ~0.43 GPa in the pressure calculation. Therefore the calculated results of the CGS $Fm\bar{3}m$-$Cmcm$ phase transition need experimental verification.

2.3.2 Solar Cell Materials upon Doping

2.3.2.1 Al-Doped $CuInSe_2$: $CuIn_{1-x}Al_xSe_2$ Structural, Electronic, and Optical Properties

Structural Properties

$CuIn_{1-x}Al_xSe_2$ crystallizes in the chalcopyrite structure, which is shown in Fig. 2.3. The chalcopyrite structure can be obtained from the cubic zinc blende structure, which contains only one type of cation. However, the presence of two different cations in the chalcopyrite structure ordered in the half tetrahedral sites yields a doubling of the zinc-blende unit cell along the c direction. In general, the bond lengths of I–VI and III–VI (denoted by d_{I-VI} and d_{III-VI}, respectively) are not equal, which can lead to a tetragonal distortion. Two structural parameters $\eta = c/a$ and $\mu = 0.25 + \left(d_{I-VI}^2 - d_{III-VI}^2\right)/a^2$, where a is the lattice constant (Å) in the x or y direction and c is in the z direction, are employed to characterize this tetragonal distortion. The structural parameter η describes a deformation of the unit cell to a length c (Å) which is generally different from $2a$ and μ describes a repositioning of the anions in the x-y plane (Å).

Electronic Properties

The calculated energy gaps are 0.31 and 1.21 eV, respectively, for $CuInSe_2$ and $CuAlSe_2$ (see Fig. 2.4), both of them are smaller than their experimental values 1.04 and 2.67 eV [26], respectively. This is because of the correlation between the valence electrons is underestimated in the GGA, and the DFT method is known to underestimate the energy gap value and overestimate the lattice constants. However, the energy gap tends to increase with the increase of Al content, which is basically the same as the experimental result (see Fig. 2.4). The compositional dependence of the band gap can be fit by Eq. (2.1)

$$E_g(x) = E_g(0) + \big(E_g(1) - E_g(0)\big)x + bx(x-1), \tag{2.1}$$

here b is the optical bowing parameter (eV), which describes the band gap variation of a composite semiconductor alloy. It is known to be related to the electronic structure and the lattice deformation in the semiconductor alloys. The least squares fit shown in Fig. 2.4 gives a value of b = 0.49.

Optical (Absorption) Properties of $CuIn_{1-x}Al_xSe_2$

The absorption coefficient indicates that the fraction of energy lost by the wave when it passes through a unit thickness of the material. The absorption spectra of

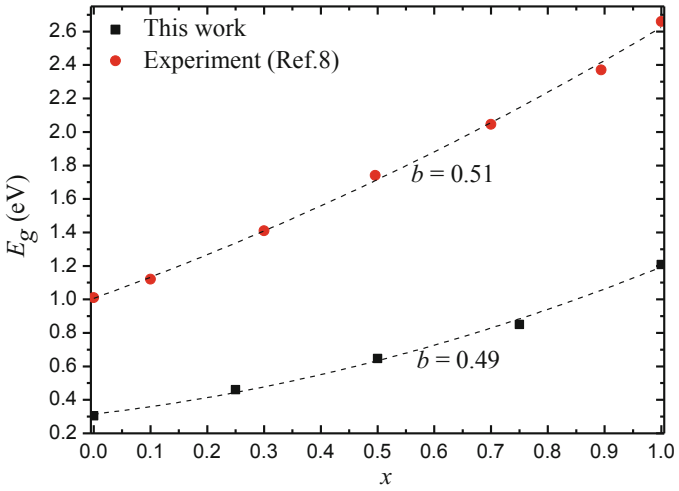

Fig. 2.4 Variation of the band energy gap of $CuIn_{1-x}Al_xSe_2$ with Al content

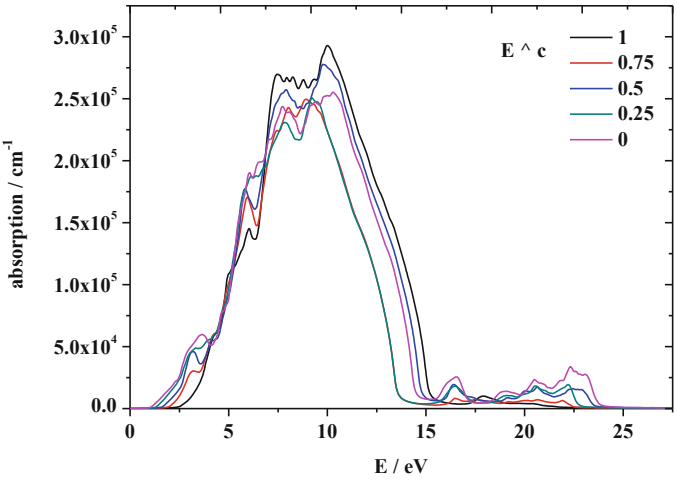

Fig. 2.5 The absorption of $CuIn_{1-x}Al_xSe_2$ in the ordinary polarization

$CuIn_{1-x}Al_xSe_2$ with five doping densities are given in Fig. 2.5. From the absorption spectra, the band gap can also be obtained. It can be found that Al reduces when the band gap is less than 4 eV, and the transparent region increases up to 2.4 eV or more than 25 eV. When the photon energy is less than 4 eV, the absorption decreases with x from 0 to 1 (cm^3). When x is 0.25 and 0.75, the absorption of $CuIn_{1-x}Al_xSe_2$ in the high energy region is almost the same, and their absorption peak is the lowest, while the pure CuAlSe2 has the highest peak.

2.3.2.2 Generalized Stacking Fault Energies and Cleavage Energies of Cu(Al/Ga/In)Se_2 and CuGa(S/Se/Te)$_2$

Generalized Stacking Fault Energies

Generalized stacking fault (GSF) energies $\gamma(\boldsymbol{u})$ in CuXSe$_2$ and CuGaY_2 compounds for fault vectors u along the directions of <110>(001), <100>(001), and <$\bar{1}$10>(112) are displayed in Fig. 2.6. As can be seen in Fig. 2.6, all the γ-curves exhibit a maximum value at u/b = 0.25 and a minimum value at u/b = 0.5, where $\boldsymbol{b}$ is the Burgers vector. These maximum and minimum values define the unstable stacking fault energies γ_{us} and the intrinsic stacking fault energies γ_{isf} of these compounds, respectively.

Values of γ_{us} along the <110>(001) direction for five compounds is lower than that of along the <100>(001) direction, which indicates that it is easier to slip along the <110> direction on the (001) plane. The values of γ_{us} along the <$\bar{1}$10>(112) direction are even lower than that value along the <110>(001) direction. Therefore, it is easiest for these compounds to slip along the <$\bar{1}$10>(112) direction among the three slip systems considered here.

γ_{isf} of CuInSe$_2$ (~0.24 J/m^2) is about an order of magnitude higher than that of the other four compounds along the <110>(001) direction. The value of γ_{isf} characterizes the possibility of a full dislocation splits into partial dislocations

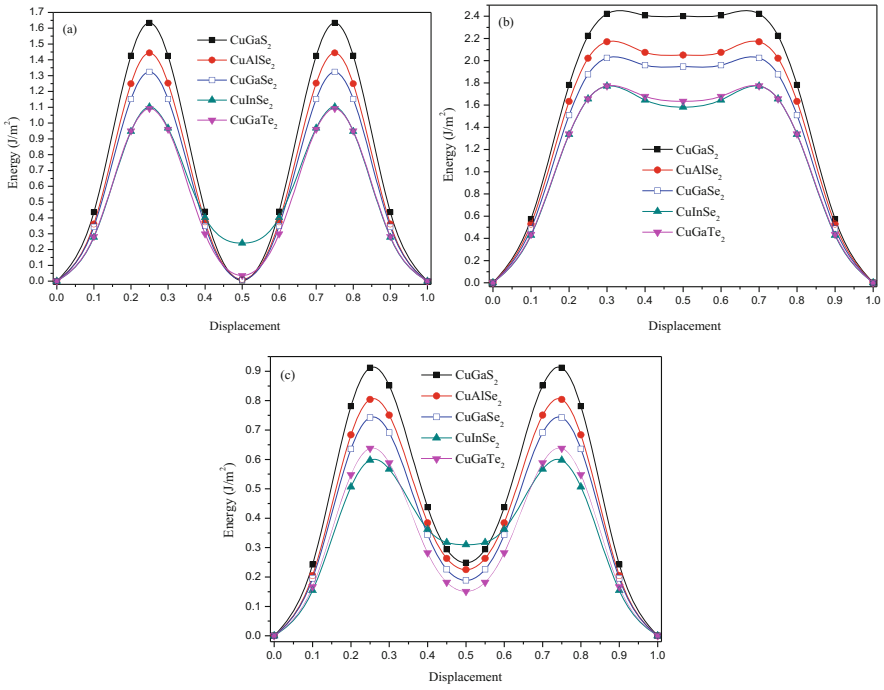

Fig. 2.6 γ-curves of CuGaS$_2$, CuAlSe$_2$, CuGaSe$_2$, CuInSe$_2$, and CuGaTe$_2$ for displacement along the directions: (**a**) <110>(001), (**b**) <100>(001), (**c**) <$\bar{1}$10>(112)

joined by a stacking fault defect. The distance between the partial dislocations is closer to the width of the dislocation core as γ_{isf} becomes larger. When γ_{isf} is large enough, the full dislocation will not split, and the motion of the full dislocation will be impeded. The values of γ_{isf} along the <100>(001) direction for five compounds is much larger than that value along the <110>(001) direction. Hence, the full dislocation <100>(001) probably has a compact core, and the tendency of the <100>(001) dislocation to split into partials is smaller than that of the <110>(001) dislocation.

γ_{isf} along the <110>(001) and $<\bar{1}10>(112)$ directions can also be called antiphase boundary (APB) energies, E_{APB}. This is because of along the two slip directions antiphase boundary defects can be formed in the sheared lattice configurations at $u/b = 0.5$. And in the configuration with an antiphase boundary defect, the copper sites at and above the slip plane are taken by group-III atoms and vice versa, while sites of a group-VI atom are not changed. γ_{isf} along the <100>(001) direction are not E_{APB}, as there are no antisites in the sheared lattice configurations at $u/b = 0.5$. Values of γ_{isf} along the <110>(001) and $<\bar{1}10>(112)$ directions also represent the possibility of formation of antiphase boundary defect in the five compounds. The low APB energies (~0.004 J/m^2 to ~0.31 J/m^2) in these compounds imply that the formation of the stable antiphase boundary defects along the <110>(001) and $<\bar{1}10>(112)$ directions are quite probable.

Both γ_{us} and γ_{isf} on the γ-curve are the key factors of influencing the plastic deformation of materials. As suggested by Gornostyrev [11], there is a critical stress intensity factor for the nucleation of a leading partial dislocation on the slip plane near the crack tip. And the critical stress intensity factor is proportional to the value of $\sqrt{\gamma_{us}}$. When the leading partial dislocation moves away from the crack, it leaves behind a stacking fault. The stacking fault facilitates to the nucleation of a trailing partial dislocation, but the leading partial always impedes the nucleation. So, there is also a critical stress intensity factor which is proportional to the value of $\sqrt{\gamma_{us} - \gamma_{isf}}$ for the nucleation of the trailing partial dislocation [11, 37]. Along the $<\bar{1}10>(112)$ direction, γ_{us} of $CuInSe_2$ (~0.6 J/m^2) is the lowest among the five compounds, while its γ_{isf} (~0.31 J/m^2) is the highest. So γ_{us}-γ_{isf} of $CuInSe_2$ (~0.29 J/m^2) should be the lowest. It means that along the $<\bar{1}10>(112)$ slip direction the critical stress intensity factors of $CuInSe_2$ for the nucleation of the leading and trailing partial dislocations are the lowest among these compounds. Hence, along with the $<\bar{1}10>(112)$ slip direction the nucleation of the leading and trailing partial dislocations is the easiest for $CuInSe_2$ among the five compounds. As a result, it is most possible for $CuInSe_2$ to undergo a dislocation-nucleation-induced plastic deformation along the $<\bar{1}10>(112)$ slip direction among the five compounds.

Cleavage Energies γ_{cl}

The cleavage energy γ_{cl} is the energy required for creating two surfaces. The cleavage energy for (112) plane of $CuInSe_2$ should be no larger than 1.28 J/m^2 and for (001) plane of $CuGaSe_2$ should be about 1.9 J/m^2. As can be seen in Fig. 2.7, the

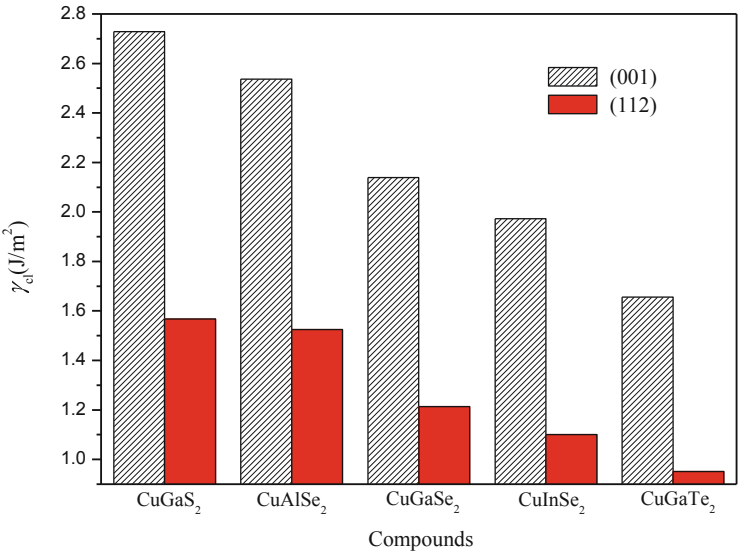

Fig. 2.7 Cleavage energies of (001) and (112) planes in $CuGaS_2$, $CuAlSe_2$, $CuGaSe_2$, $CuInSe_2$, and $CuGaTe_2$

results show that the cleavage energy for (112) plane of $CuInSe_2$ and for (001) plane of $CuGaSe_2$ is 1.1 J/m^2 and 2.14 J/m^2, respectively. In Fig. 2.6, it is obvious that γ_{cl} of (112) plane is lower than that of (001) plane for any of the five compounds. Therefore, (112) plane is the preferable plane for fracture in these compounds. And from Fig. 2.7, one can see that γ_{cl} of (001) and (112) planes decrease with increasing atomic radius in the CuXSe2 compounds (X: Al ! Ga ! In) and in the CuGaY2 compounds (*Y*: S → Se → Te) (Tellurium, Te).

2.3.3 Atomistic Distribution in Solar Cell Materials

2.3.3.1 Temperature Effects on Distribution and Inhomogeneous Degree of In-Ga Atoms in $CuIn_{1-x}Ga_xSe_2$ Alloys

In Fig. 2.8, to make the observation easier, Cu and Se atoms are not displayed in the snapshots. It is seen that there is a segregation of In and Ga atoms in CIGS alloys when the temperature is low, while the In-Ga distributions become homogeneous at the high temperature. The clustering of Ga or In atoms in CIGS alloys with different Ga contents exists in a spherical, rod-like, lamellar or a massive structure at the low temperature. It is very possible to prepare CIGS-based quantum dots (QDs) at low temperatures via the phase-separation found here because the growth of QDs by phase-separation has already been established for the similar material InGaAs.

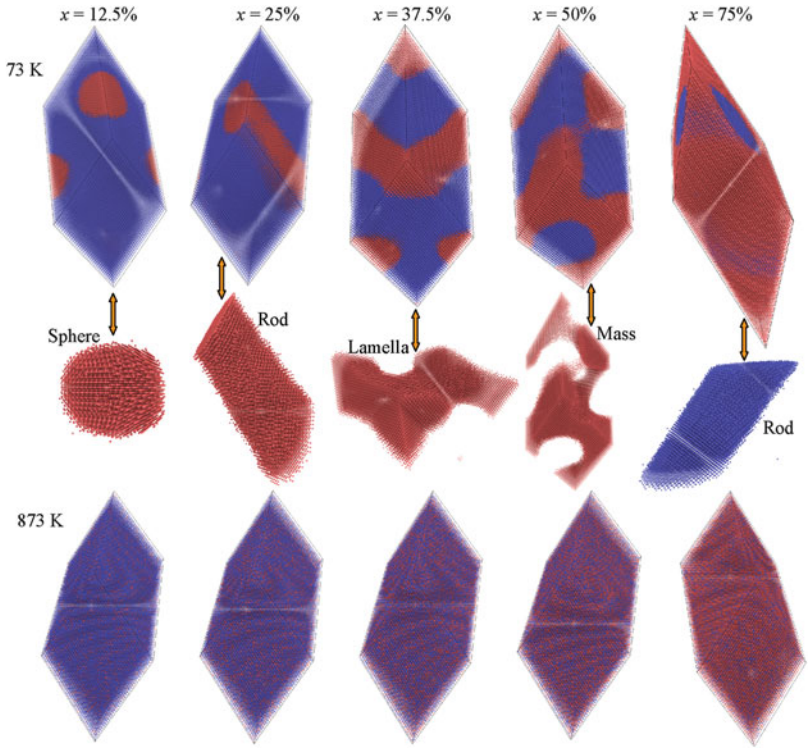

Fig. 2.8 Snapshots of the In-Ga distributions in $CuIn_{1-x}Ga_xSe_2$ alloys at 73 K (upper row) and 873 K (lower row). Blue and red balls represent the In and Ga atoms, respectively. The middle row shows the morphologies of Ga(In) clustering in corresponding CIGS supercells at 73 K. (For interpretation of the references to color in this figure legend, the reader is referred to the web version of this article)

2.3.3.2 Effect of Temperature on Atomic Distribution and Inhomogeneity in $CuIn(Se_{1-x}S_x)_2$ Alloys

The Distribution Morphologies of Se-S Atoms in $CuIn(Se_{1-x}S_x)_2$ Alloys

Figure 2.9 shows the distribution morphologies of Se-S atoms in $CuIn(Se_{1-x}S_x)_2$ (CISS) alloys at the typical temperatures of 48 K, 110 K (low temperatures), and 773 K (high temperature), respectively, because of the distribution morphologies of Se-S atoms in CIGS alloys are similar at low or high temperatures. To make the observation easier, both Cu and In atoms are not displayed in the snapshots, and the distribution morphologies of simplex S(Se) atoms in CISS alloys are further shown by deleting all Se(S) atoms. From Fig. 2.9, it can be observed that there is a segregation of S and Se atoms in CISS alloys both at 48 K and 110 K, which means that there is a phase separation of $CuInSe_2$ (or Se-rich CISS) and $CuInS_2$ (or S-rich CISS) in CISS alloys at low temperatures. This result agrees well with the phase diagram of CISS alloys (Xue et al. 2014) calculated by us. When the temperature

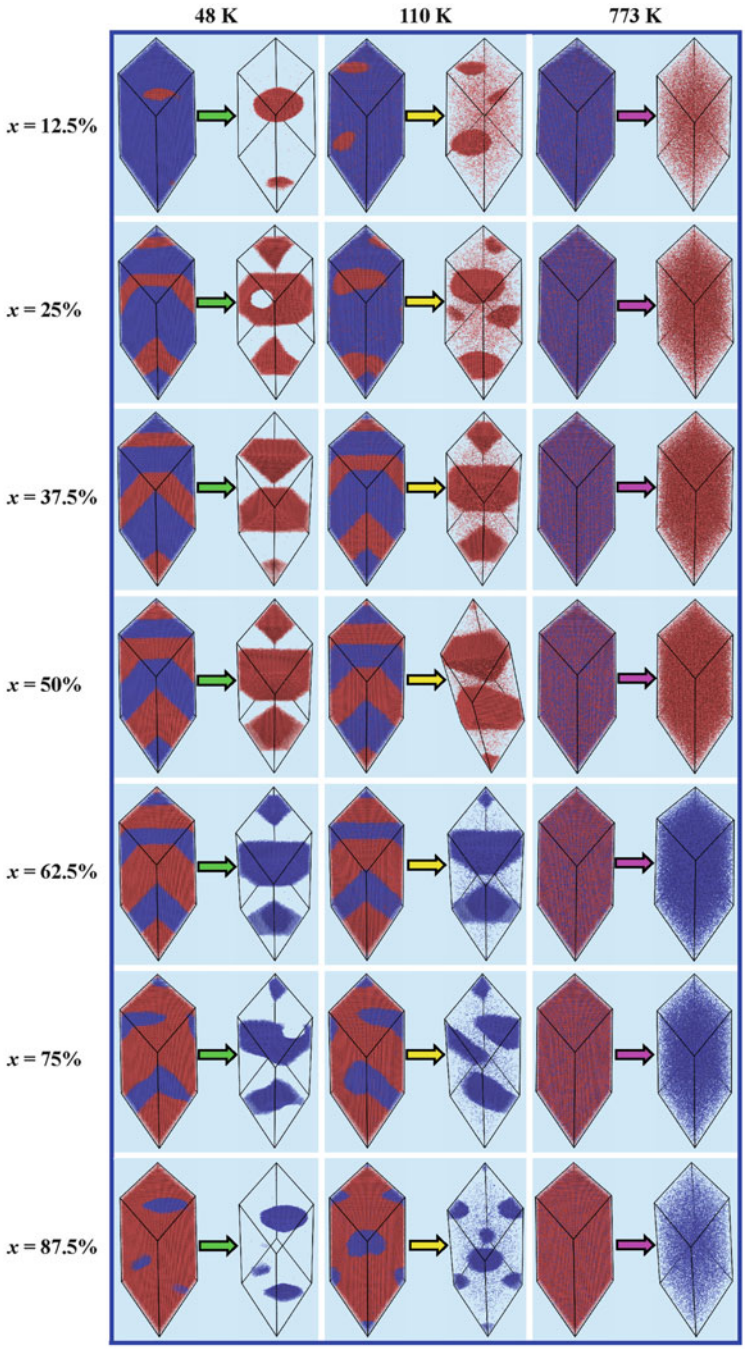

Fig. 2.9 Snapshots of the Se-S distributions in $CuIn(Se_{1-x}S_x)_2$ alloys with x = 12.5%, 25%, 37.5%, 50%, 62.5%, 75%, and 87.5% at the temperatures of 48 K, 110 K, and 773 K are shown on the left side of the green, yellow, and magenta arrows, respectively. Red and blue balls represent S

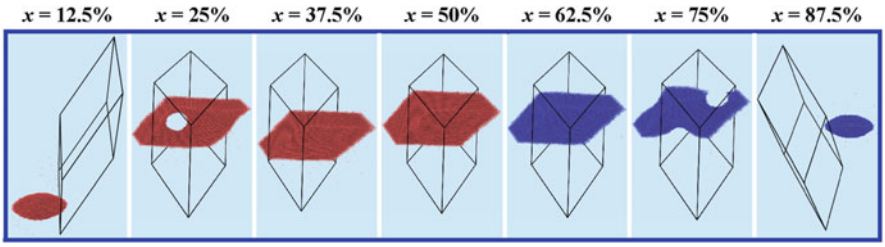

Fig. 2.10 The distribution morphologies of S(Se) atoms in $CuIn(Se_{1-x}S_x)_2$ alloys with $x = 12.5$, 25, 37.5, 50, 62.5, 75, and 87.5% respectively at 48 K, which can be obtained by translating the S (Se) atoms shown on the right side of the green arrows in the column of 48 K of Fig. 2.3 according to the periodicity. Red and blue balls represent S and Se atoms, respectively

rises from 48 K to 110 K, more S(Se) atoms are scattered around. And the Se-S distributions seem to be homogeneous when the temperature is 773 K. As a result, the Se-S distribution in CISS alloys becomes more and more homogeneous as the temperature is raised from the low temperature to relatively high temperature.

As shown in Fig. 2.10, to better observing the distribution morphologies of S (Se) atoms in CISS alloys at 48 K, the S(Se) atoms in supercells were translated periodically. The distribution morphologies are shown in Fig. 2.10, which are equivalent to that shown on the right side of the green arrows in the column of 48 K of Fig. 2.9. It is seen that the clustering of S(Se) atoms in CISS alloys exists in an ellipsoidal or a lamellar structure at 73 K. When the concentration of S(Se) atoms is less than 12.5%, the S(Se) atoms in CISS alloys should cluster in a form of ellipsoids or spheres. As the concentration of S(Se) atoms increases from 12.5% to 25%, the clustering of S(Se) atoms in CISS alloys changes from ellipsoids to lamellas with holes which should be filled with Se(S) atoms. The clustering of S (Se) atoms keeps lamellar as the concentration of S(Se) atoms increases from 25% to 50%, meanwhile the thickness of the lamellas increases. Therefore, for CISS alloys with $x = 25$, 37.5, 50, 62.5, and 75% respectively, the microstructures will appear in periodic patterns consisted of alternate S-rich and Se-rich CISS lamellas at low temperatures, which is a characteristic feature of the phase separation.

2.3.3.3 Phase Diagram of the $CuInSe_2$-$CuGaSe_2$ Pseudobinary System

Figure 2.11 shows the calculated dependence of the total energy E against volume V for $CuIn_{1-x}Ga_xSe_2$. By fitting the E-V data points to the Birch-Murnaghan EOS one can obtain the equilibrium volume V0 and the equilibrium total energy E0 of CIGS for a different fraction of Ga. In view of the complexity of the SQSs of CIGS, the dependence of V0 on the composition instead of the lattice constant was plotted, as shown in Fig. 2.12. And the equilibrium volumes of CIGS we calculated are

Fig. 2.9 (continued) and Se atoms, respectively. The distribution morphologies of S(Se) atoms in CISS alloys at 48 K, 110 K, and 773 K are shown on the right side of the green, yellow, and magenta arrows, respectively

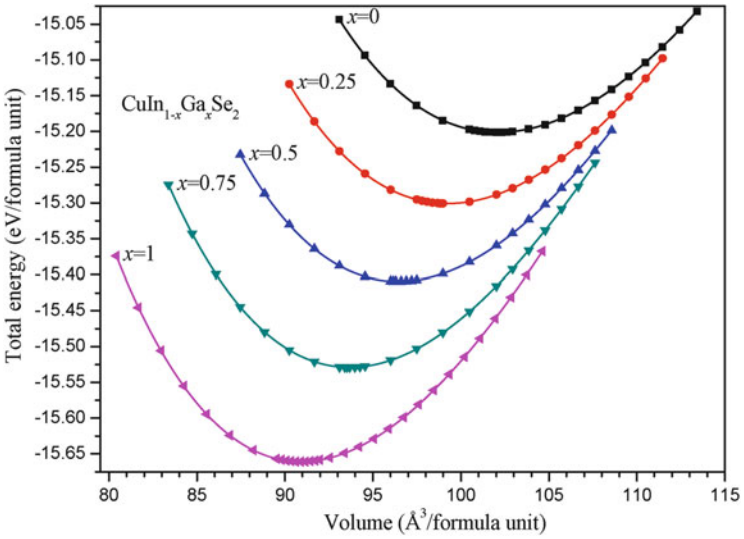

Fig. 2.11 The dependence of the total energy on volume for the $CuIn_{1-x}Ga_xSe_2$ alloys

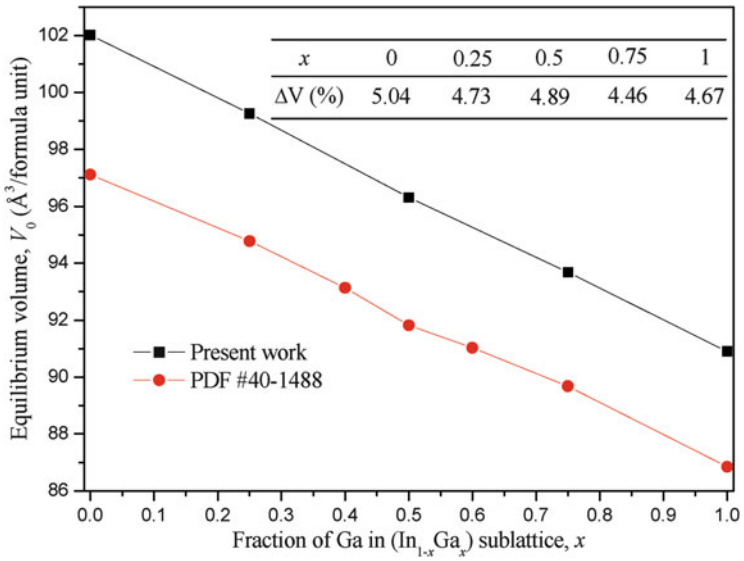

x	0	0.25	0.5	0.75	1
ΔV (%)	5.04	4.73	4.89	4.46	4.67

Fig. 2.12 The calculated equilibrium volume of $CuIn_{1-x}Ga_xSe_2$ as a function of the Ga fraction x: a comparison with the powder diffraction file (PDF) 40-1488. The inserted table shows the volume error percentages for a different fraction of Ga

overestimated compared with those of experimental data (PDF #40-1488). The errors, $\Delta V = (V0 - VExperiment)/VExperiment$, are no larger than 5.04%; all of these are within the errors usually obtained by DFT-PBE calculations.

In order to determine the Gibbs free energy of mixing of the $CuIn_{1-x}Ga_xSe_2$ solid solution with respect to the isostructural terminal phases, we have to calculate the interaction parameter $\Omega(x)$ first. The isostructural CIS and CGS were chosen as the terminal phases for CIGS. The interaction parameter $\Omega(x)$ can be obtained from Eqs. (2.2) and (2.3), that is,

$$\begin{aligned} &E(CuIn_{1-x}Ga_xSe_2) - [(1-x)E(CuInSe_2) + xE(CuGaSe_2)] \\ &\quad = x(1-x)\Omega(x). \end{aligned} \tag{2.2}$$

$$\Omega(x) = \alpha x^2 + \beta x + \gamma. \tag{2.3}$$

Figure 2.13a shows the Gibbs free energy (kJ/mol) of mixing of $CuIn_{1-x}Ga_xSe_2$, ΔGmix, as a function of x at a given absolute temperature of 360 K. Figure 2.13b shows the temperature-composition phase diagram derived from the curves of Gibbs free energy of mixing. The binodal curve denotes the equilibrium solubility limits of the solid solution and is defined by the condition at the chemical of all solution components is equal in each phase. In general, the binodal can be determined at a given temperature by drawing a common tangent line to the curve of Gibbs free energy of mixing, as shown in Fig. 2.13a for T = 360 K. The spinodal is the limit of stability of the solution and can be determined as the curve of the second derivative of Gibbs free energy of mixing with respect to the Ga fraction is zero, that is, $\partial^2(\Delta\text{Gmix})/\partial x^2 = 0$ (see Fig. 2.13a). Inside the spinodal curve, where $\partial^2(\Delta\text{Gmix})/\partial x^2 < 0$, the thermodynamically driving phase segregation occurs without any activation; therefore, the mixture of two phases of $CuInSe_2$ and $CuGaSe_2$ (or In-rich CIGS and Ga-rich CIGS) is stable in this region. Between the spinodal and binodal curves, where $\partial^2(\Delta\text{Gmix})/\partial x^2 > 0$, the phase segregation occurs by activated nucleation and growth, and this region is also known as the metastable phase region. Outside the binodal curve, the single-phase CIGS is stable.

From Fig. 2.13b one can see that the CIS-CGS pseudobinary system exhibits the phase separation at low temperature. The binodal curve gives the consolute temperature Tc (the critical temperature above which the components of a mixture are miscible in all proportions) of 485 K for CIGS alloys, and the Ga concentration associated with Tc, xc, is about 0.804 (mole fraction). Our result shows that it is possible to obtain the homogeneous CIGS phase in the whole Ga concentration range at relatively low temperature under equilibrium growth conditions. Here, one should also note that in practice to overcome the energy barrier for the diffusing of atom and shortening the time of atom growth time, it is usually required to increase the growth temperature intentionally for most of the growth conditions.

In Fig. 2.13b, it is important to note that both the binodal and spinodal curves are significantly asymmetric, and on both curves, there is an unusual local between maximum and minimum. This phenomenon occurs at temperatures lower than 500 K, the regime where data are difficult to obtain experimentally due to slow kinetics. As shown in Fig. 2.13b, the temperature of both the equilibrium solubility limit and the stability limit for $CuIn_{0.25}Ga_{0.75}Se_2$ is higher than that of for $CuIn_{0.75}Ga_{0.25}Se_2$. It means that the temperature range where two phases may

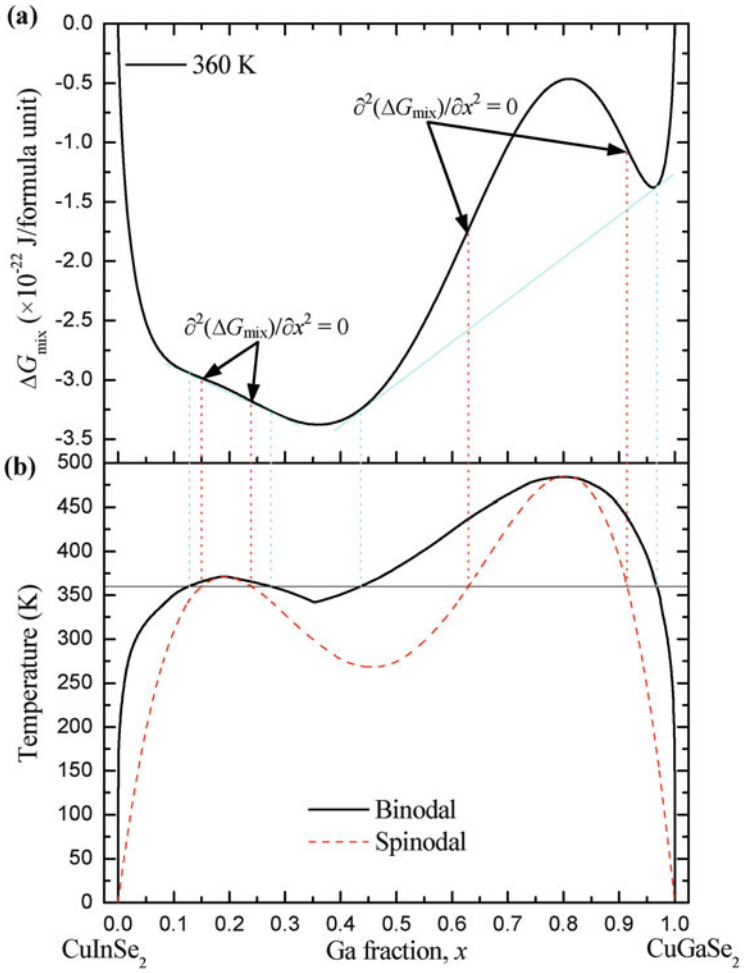

Fig. 2.13 (**a**) Gibbs free energy of mixing of the $CuIn_{1-x}Ga_xSe_2$ solid solution as a function of Ga fraction, x, at $T = 360$ K. (**b**) Calculated temperature-composition phase diagram for $CuIn_{1-x}Ga_xSe_2$ with $CuInSe_2$ and $CuGaSe_2$ chosen as reference states. The binodal (solid line) is defined by the points at which a common tangent line touches the curve of Gibbs free energy of mixing, and the spinodal (dashed line) is determined as the curve of which the second derivative of Gibbs free energy of mixing with respect to the Ga fraction is zero

coexist in thermal equilibrium (i.e., the inhomogeneous region) for the former is wider than that for the latter. In a particular case where the temperature is 400 K, the $CuIn_{0.75}Ga_{0.25}Se_2$ has been homogeneous as it is outside the binodal curve, and $CuIn_{0.25}Ga_{0.75}Se_2$ is still inhomogeneous as it is located in the spinodal curve. Therefore, it is understandable that the inhomogeneous degree of $CuIn_{0.25}Ga_{0.75}Se_2$ is larger than that of $CuIn_{0.75}Ga_{0.25}Se_2$ when compared them at the same temperature.

One should keep in mind that the phase diagram shown in Fig. 2.13b is calculated with the temperature-independent interaction parameter. And it does not consider the short-range order existing in the solid solution as well as the phonon contribution to the free energy. Any improvement such as using larger unit cells, a temperature-dependent interaction parameter, a more accurate treatment of the entropy of mixing, a self-consistent determination of the short-range order, and so on can make the calculating phase diagram more accurate.

2.3.3.4 Phase Equilibrium of a $CuInSe_2$-$CuInS_2$ Pseudobinary System

The calculated phase diagram of $CuIn(Se_{1-x}S_x)_2$ alloys is shown in Fig. 2.14, where the miscibility gaps (binodal curves) correspond to the coexistence of two stable phases. Inside the miscibility gaps, the phase separation occurs, and the mixture of two phases of $CuInSe_2$ and $CuInS_2$ is stable. Outside the miscibility gaps, single-phase homogeneous $CuIn(Se_{1-x}S_x)_2$ is stable. In this study, the consolute temperature (the critical temperature, above which the components of a mixture are miscible in all proportions), T_C predicted by the conventional cluster expansion without vibrational contribution is 170 K, and the corresponding concentration associated with T_C, X_C is about 0.61 (mole fraction). The miscibility gap is asymmetric. And the result also shows that the CISS alloys can exhibit the phase separation at low temperature; the tendency to phase separation can cause alloy inhomogeneity to some extent. To confirm the calculation method and result, the phase diagram of $Cu(In_{1-x}Al_x)Se_2$ alloys, in the same way, is calculated and compared with available data reported, as shown in the inset of Fig. 2.14.

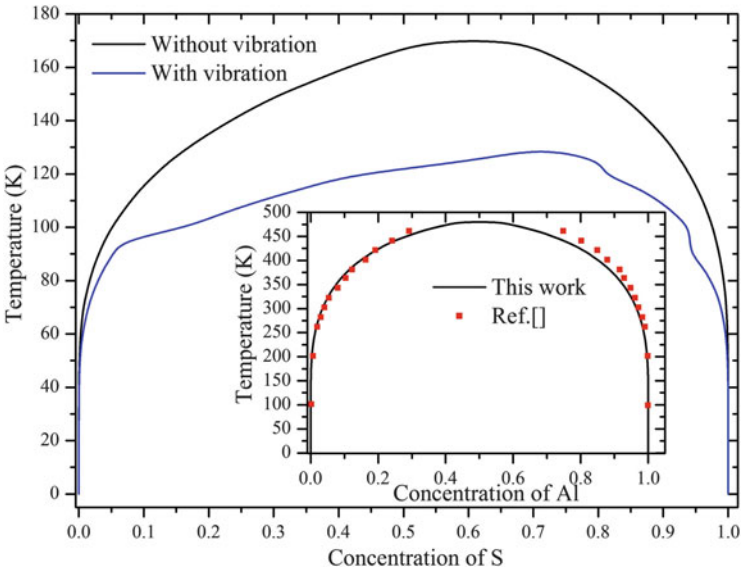

Fig. 2.14 The calculated phase diagrams of $CuIn(Se_{1-x}S_x)_2$ and $Cu(In_{1-x}Al_x)Se_2$ (inset) alloys

From the inset of Fig. 2.14, one can see that the binodal curve of $Cu(In_{1-x}Al_x)Se_2$ calculated is in close agreement with the data calculated by Kumagai et al. [18]. And the consolute temperature of $Cu(In_{1-x}Al_x)Se_2$ alloys is 480 K, only of 20 K higher than the result (460 K) obtained by Kumagai et al. [18]. This indicates that the calculation method is reasonable and the calculated phase diagram of CISS alloys should be reliable. Moreover, the consolute temperature is 170 K for $CuInSe_2$-$CuInS_2$ system, suggesting that CISS alloys are stable at typical growth temperatures. It should be noted that the low temperature of the miscibility gap can partly contribute to the accuracy of the cluster expansion. Because the effective cluster interactions (ECIs) can be modified by considering structures with more atoms, this is likely to influence the calculated phase boundary. However, as the slow atomic diffusion at low temperatures often prevents the direct observation of phase separation, the miscibility gap predicted by first-principles calculations is very likely to be overlooked in the experiments due to low temperature and slow kinetics.

2.3.3.5 Sulfur-Selenium Segregation in $ZnSe_{1-x}S_x$: The Role of Lattice Vibration

Phase Diagram of $ZnSe_{1-x}S_x$

The phase diagrams of $ZnSe_{1-x}S_x$ alloys computed with and without lattice vibration effects are shown in Fig. 2.15, where the miscibility gaps (binodal curves) correspond to the coexistence of two stable phases. Inside the miscibility gaps, the phase separation occurs, and the mixture of two phases of zinc selenide (ZnSe) and zinc sulfide (ZnS) is stable. Outside the miscibility gaps, single-phase homogeneous

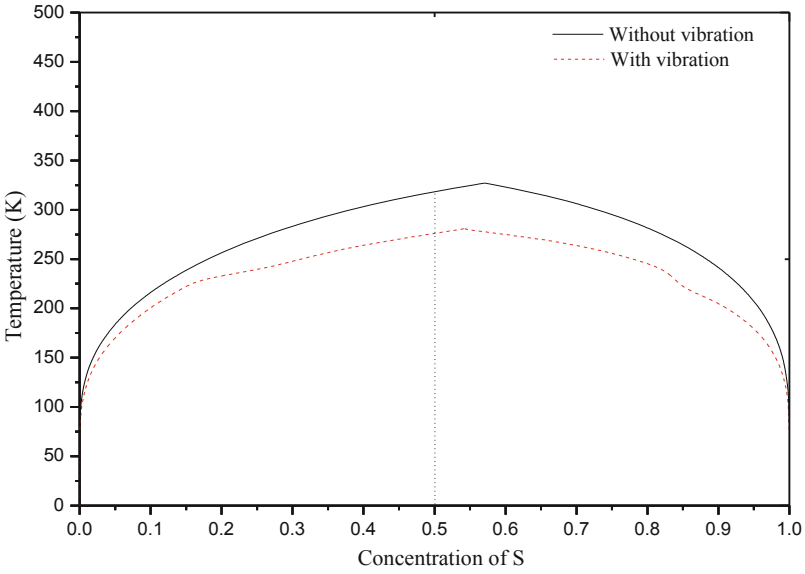

Fig. 2.15 The calculated phase diagram of $ZnSe_{1-x}S_x$ alloys

$ZnSe_{1-x}S_x$ is stable. As shown in Fig. 2.15, the consolute temperature T_c predicted without vibrational contribution is 327 K ($x_c = 0.571$ mole fraction). The $ZnSe_{1-x}S_x$ system exhibits slight asymmetry, with maximum closer to the end member ZnS. The result also shows that the $ZnSe_{1-x}S_x$ alloys can exhibit the phase separation at low temperature; the tendency to phase separation can cause alloy inhomogeneity to a certain extent.

Figure 2.15 also explains that the contribution of lattice vibrations reduces the consolute temperature to 281 K ($x_c \approx 0.543$). And the miscibility gap is also asymmetric. The x_c with the vibrational effect (0.543) is smaller than that without the vibrational effect (0.571). The miscibility gap with considering the effect of vibration exhibits subtle increase symmetry than that without considering the effect of vibration. Such results about the critical temperatures are in agreement with the few available experimental findings on the coexistence curves of such alloys and indicate the complete miscibility of the $ZnSe_{1-x}S_x$ system.

Distribution of S and Se Atoms in $ZnSe_{1-x}S_x$ Alloys

As shown in Fig. 2.16, at low temperature, for example, at 250 K, obvious phase separation between ZnS and ZnSe can be observed in $ZnSe_{0.5}S_{0.5}$ alloy, which means that there are two phases in $ZnSe_{0.5}S_{0.5}$ alloy: a rich-S and a poor-Se $ZnSe_{1-x}S_x$ phase. As temperature increasing, $ZnSe_{0.5}S_{0.5}$ becomes more homogeneous especially over 300 K. Similar observation can also be found in the right part of the Fig. 2.16 which shows the spatial distribution of S and Se atoms in $ZnSe_{0.5}S_{0.5}$ alloy with lattice vibration effects.

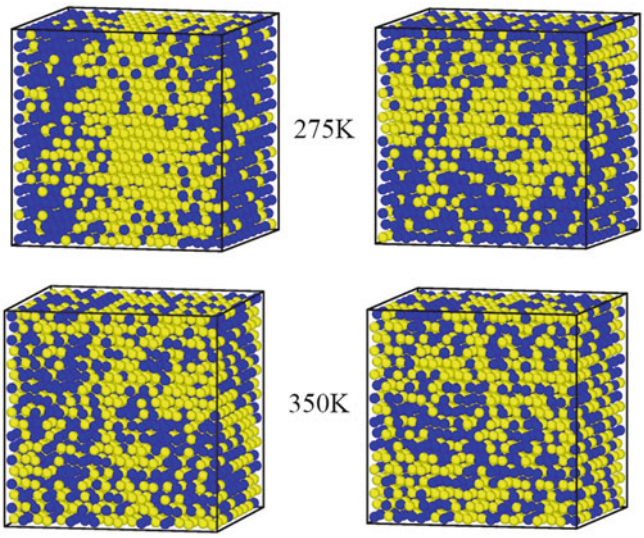

Fig. 2.16 Snapshot of the $ZnSe_{0.5}S_{0.5}$ with (on the right) and without (on the left) lattice vibration effects at the temperature of 275 K and 350 K. Yellow and blue spheres represent S and Se atoms, respectively

2.3.4 Interfaces in Solar Cells

2.3.4.1 Cu_2ZnSnS_4/WZ-ZnO Interface

Interface Structural and Electronic Properties

Figure 2.17a shows the copper zinc tin sulfur/*W*urtzite structure zinc oxide (Cu_2ZnSnS_4/WZ-ZnO) interface model. The optimized parameters of CZTS/WZ-ZnO interface model are $a = 10.66$ Å, $b = 5.56$ Å, $c = 57.53$ Å. This interface has two possible bonding types (see Fig. 2.1b–c, A1 to B1 or A2 to B2) called model A. The interface distance can be obtained by adopting single point energy calculation method. When the interlayer distance is 2.044 Å and 2.099 Å, the model A and the model B interface has the lowest interface total energy, respectively. The binding energy for model A and model B interface system is -0.21 J/m^2 and -0.19 J/m^2, respectively. The result indicates that model A interface system is slightly more stable than model B interface.

Figure 2.18a shows the total density of states (TDOS) of CZTS (1 0 2)/WZ-ZnO (1 1 0) interface. New electronic states appear near the Fermi level, and these are so-called interface states. Further analysis indicates that the local density of states (LDOS) of CZTS layer 1 and WZ-ZnO layer 1 are contributed to the interface states from 0.5 eV to 0.9 eV. In addition, compared to the LDOS of WZ-ZnO layer 5, the LDOS of WZ-ZnO layer 1 also has a density peak at about -0.7 eV to -0.2 eV.

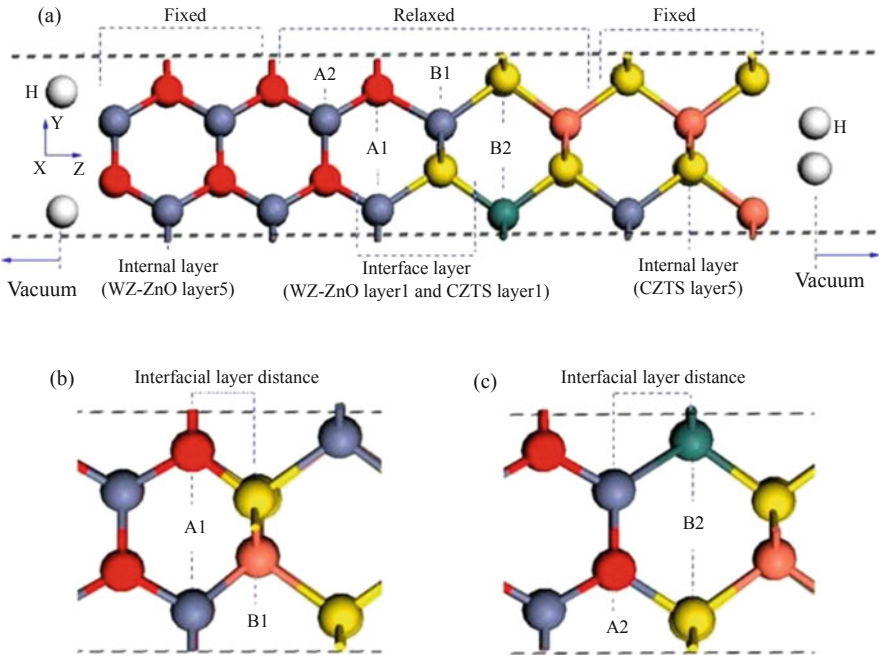

Fig. 2.17 Schematic diagram of CZTS (1 0 2)/WZ-ZnO (1 1 0) interface model (**a**), the interface bonding style of model A (**b**) and bonding style of model B (**c**)

Figure 2.18f–k are the partial density of states (PDOS) of Cu, Zn, Sn, S atoms on CZTS layer 1, respectively. The PDOS of Zn and O atoms on WZ-ZnO layer 1 are shown in Fig. 2.18j and k. There are some hybridizations of Cu-3*d* orbital with S-3*p* orbital from −4.1 eV to −0.2 eV, S-3*p* with Sn-5 *s* orbital at about 0.5 eV to 0.9 eV through comparing Fig. 2.18f with i. By comparing Fig. 2.18j with k, we see that Zn-4 *s* also has hybridization with O-2*p* from −4.8 eV to −1.5 eV.

Figure 2.19a is the general charge transfer in the interface system. Figure 2.19b is the partially enlarged charge transfer view on the interface. Figures 2.20a and 2.4b is the cross-section difference density charge of CZTS layer1 and WZ-ZnO layer 1 at the interface. The yellow color represents positive (means electron gain), and the mint green color represents negative (means electron loss). The electrons are redistributed on the interface atoms (in Fig. 2.19b), while atoms far away from the interface have less electron transfer than those on the interface (Fig. 2.19a).

Origins of the Interface States

Electron numbers are marked of each atom at the interface after relaxation, as shown in Figs. 2.19b and 2.20a and b. For the bulk CZTS, the S atoms gain about 0.81 *e*,

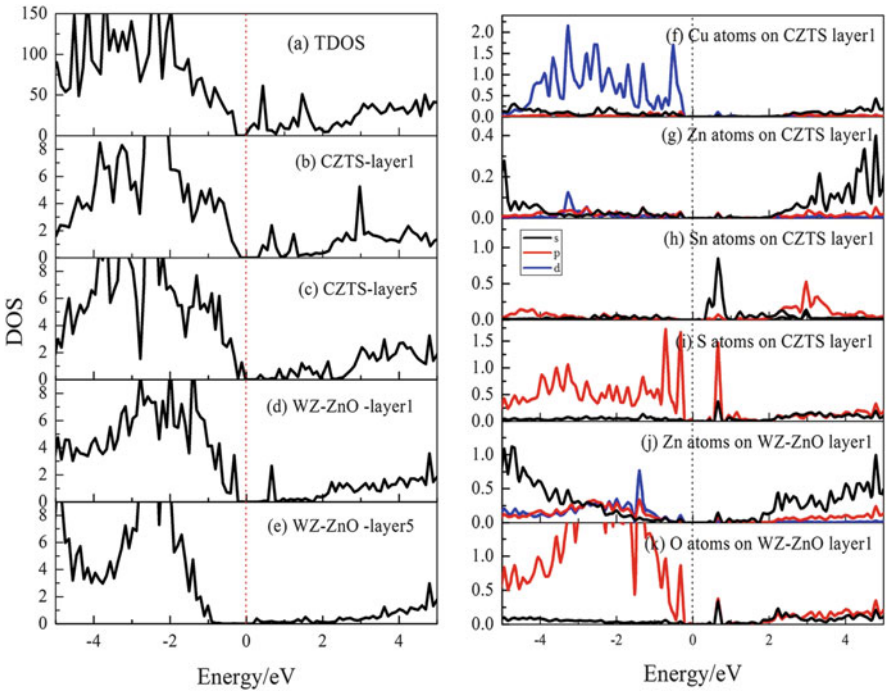

Fig. 2.18 The total density of states of CZTS (1 0 2)/WZ-ZnO (1 1 0) model A interface; local density of states on CZTS layer5 (b) and layer1 (c); local density of states on WZ-ZnO layer 1 (d) and layer 5 (e); partial density of states of Cu (f), Zn (g), Sn (h), S (i) atoms on CZTS layer 1; partial density of states of Zn(j) and O (k) atoms on WZ-ZnO layer1

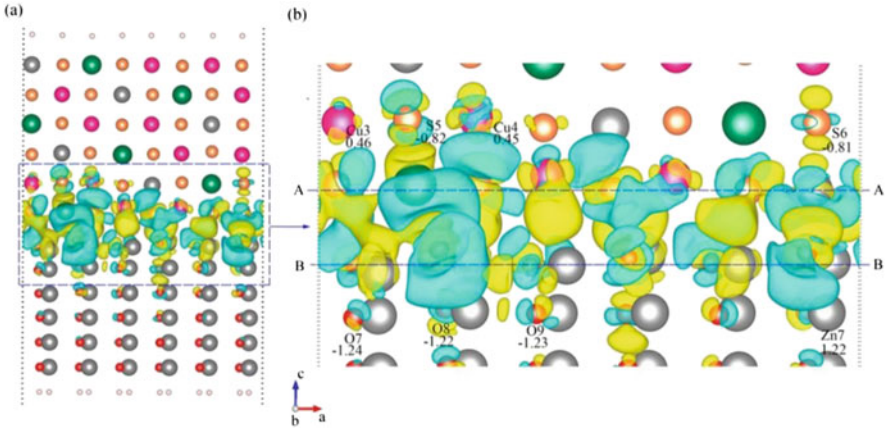

Fig. 2.19 The difference density charge (**a**); the partial enlarged view of CZTS (1 0 2)/WZ-ZnO (1 1 0) interface (**b**)

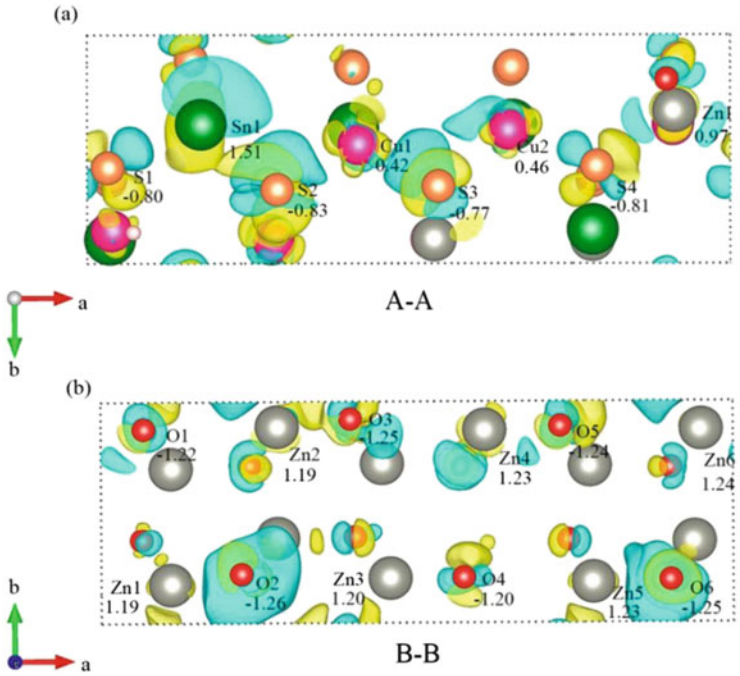

Fig. 2.20 The cross-section difference density charge of CZTS layer1 (**a**) and WZ-ZnO layer1 (**b**) at the interface

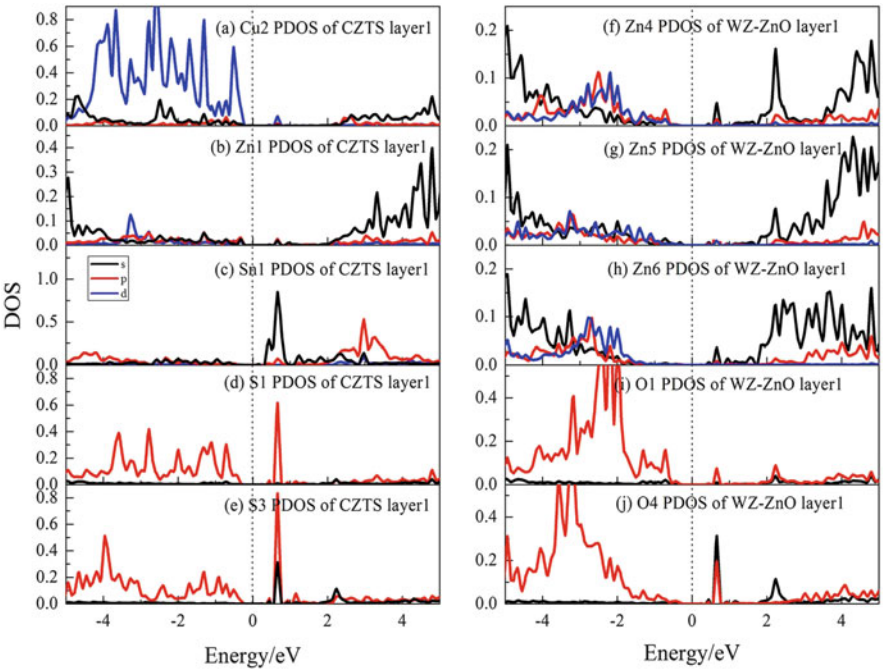

Fig. 2.21 The partial density of states of Cu2 (a), Zn1 (b), Sn1 (c), S1 (d), S3 (e) atom on the CZTS layer1 and O1 (f), O4 (g), Zn4 (h), Zn5 (i), Zn6 (j) atoms on the WZ-ZnO layer1

and Cu, Zn, and Sn atoms lose about 0.45, 0.88, and 1.47 *e*, respectively. These results indicate that the electron number transferred from Sn atoms to S atoms and from Zn atoms to S atoms is larger than that of Cu atoms to S atoms. Hence, Sn-S and Zn-S bonds are more ionic than Cu-S bonds. In bulk WZ-ZnO, Zn atoms and O atoms lose and gain about 1.23 *e*, respectively.

From CZTS layer1, Cu, Zn, and Sn atoms lose about 0.42 (or 0.46), 0.97, and 1.51 *e*, respectively. The S atoms gain about 0.77, 0.80, 0.83, and 0.81 *e*. These results indicate that the Cu atoms on the CZTS layer 1 lose fewer electrons compared with the corresponds values in the bulk. The Zn atoms on the CZTS layer 1 lose more electrons compared with the corresponds values in the bulk. Most of S atoms on the CZTS layer 1 gain fewer electrons compared with the corresponds values in the bulk. These results show that the Cu-S bonds tend to be more covalent and the Zn-S and Sn-S bonds tend to be more ionic than those in the bulk. Zn and O atoms in the WZ-ZnO layer 1 have almost same Bader's atomic charges as them in the WZ-ZnO bulk. That is to say, the bonding behavior of Zn-O is same as that in WZ-ZnO bulk.

Figure 2.21a–j show the PDOS of Cu2, Zn, Sn, S1, S3, O1, O4, Zn4, Zn5, and Zn6 atoms at the interface. From Fig. 2.21a–e, we can see that on the CZTS layer 1 the interface states are derived from 3*d*-orbital of Cu2 atom, 5 *s*-orbital of Sn atom,

3*s*-orbital of S1 atom, and 3*s*- and 3*p*-orbital of S3 atom, respectively. On the WZ-ZnO side (see Fig. 2.21f–j), the interface states are caused by 4*s*-orbital of Zn4 and Zn6 atoms, 3*d*-orbital of Zn5 atom, 2*s*-orbital of O1 atom, and 2*s*- and 2*p*-orbital of O4 atom, respectively.

As discussed above, the model A interface has high-density interface states near the Fermi level. The interface bonding (-0.21 J/m^2) and electron transfers are lower than previous values in Mo/$MoSe_2$ (-1.2 J/m^2) [49], $CuInS_2$/MoS_2 (-0.65 J/m^2) [22], and WZ-ZnO/CdS (-0.61 J/m^2) [4, 5] interfaces. From the values of interface bonding energies, the CZTS/WZ-ZnO interface is relatively less stable. The atoms near the interface are not fully bonded with each other. All of these factors lead to CZTS/WZ-ZnO to a poor quality interface for high-efficiency solar cells.

2.3.4.2 Cu_2ZnSnS_4/WZ-ZnO Interface States Passivation Mechanism

Figure 2.22a shows the total density of states (TDOS) of CZTS/WZ-ZnO interface. At the interface, there are four interfacial peaks at about 0.1–1.0 eV, labeled as P1, P2, P3, and P4. These four peaks are mainly derived from Sn and a few from O and S

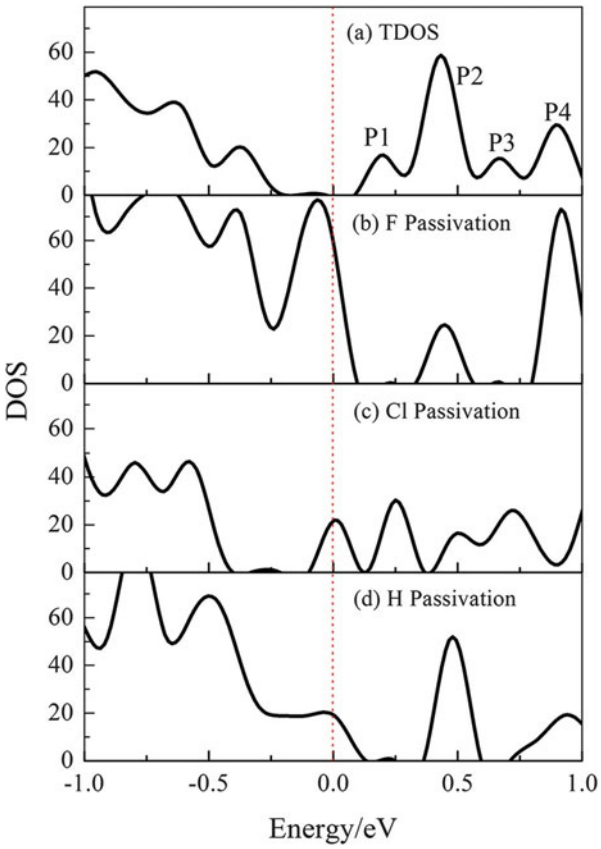

Fig. 2.22 The total density of states (TDOS) of CZTS/WZ-ZnO interface without passivation (a), and with F (b), Cl (c), and H (d) passivation

atoms on the CZTS first layer. The biggest peak P2 is derived from 5*s*-orbital of Sn atom and 3*p*-orbital of S atom.

Figure 2.22b is the TDOS after F passivation Sn atom on CZTS first layer. It is found that P1 and P3 are removed, and P2 is reduced. However, P4 becomes stronger than that without F passivation. For Cl passivation, it is found that just P2 becomes lower than that without Cl passivation, while P1, P3, and P4 are identical (in Fig. 2.22c). When H atom passivates the interface, P1 and P3 peaks are eliminated, and P2 and P4 peaks are also reduced (in Fig. 2.22d). The results suggest that interfacial density state peaks can be reduced by F, Cl, and H atom passivation. Comparing Figs. 2.22b and d with Fig. 2.22c, we know that the P1 and P3 peaks are removed; the P2 peak is reduced by F and H atoms passivation. While the P1 and P3 peaks are identical, just P2 peak reduced by Cl atom passivation. So, one can make a conclusion that H and F may have a more effective passivation effect than Cl atoms.

The Bader atomic charge and charge density difference are calculated to explore the electron transferring with and without F, Cl, and H passivation. Figure 2.23a shows that the electrons are redistributed on the interface atoms. The Sn atoms lose electrons (mint green color). The Bader atomic charge of Sn atom is 1.47 and 1.51 electrons (*e*) in bulk CZTS and in CZTS first layer, respectively. After F, Cl, and H passivation, the Bader atomic charge of Sn is 1.59, 1.51, and1.44 *e*, respectively. The Bader atomic charge of Sn changes slightly compared with that in the bulk of the interface. The Bader atomic charge of F, Cl, and H atoms are −0.74, −0.33, −0.32 *e*, respectively. The results show that F, Cl, and H atoms get about 0.74, 0.33, and 0.32 *e* after passivation, respectively. The total electrons of the interface are kept unchanging, while the passivation atoms (F, Cl, H) get electrons. Combining the results of Fig. 2.22a–d and Fig. 2.23a–d, it is known that F, Cl, and H can get the electrons of Sn which may lead to interface states. So the interface states can be passivated by F, Cl, and H atoms. The three atoms cannot fully remove the interface states for the new states not only deriving from Sn, but they also from the S and O atoms on CZTS layer 1.

2.4 Conclusions

This chapter summarized some simulations by first-principles calculations for $CuInGaSe_2$ (CIGS) solar cell materials. Under high pressure, upon doping, the lattice structure and mechanics, the optical, and the electrical properties were provided. In addition, interface states in $CuInGaSe_2$ thin-film solar cell were investigated to maximally weaken the negative impacts of interface states. The local structures and electronic properties of the interfaces were calculated. These simulations are helpful to understand the relationship between the local structures and the local atomic distribution in the solar cell materials and near the interfaces and are also useful to reveal the micro-mechanism of photoelectric changes introduced by interface states. These chapter indicates that the theoretical calculation becomes a powerful tool to understanding and to improving the $CuInGaSe_2$ solar cell's performances.

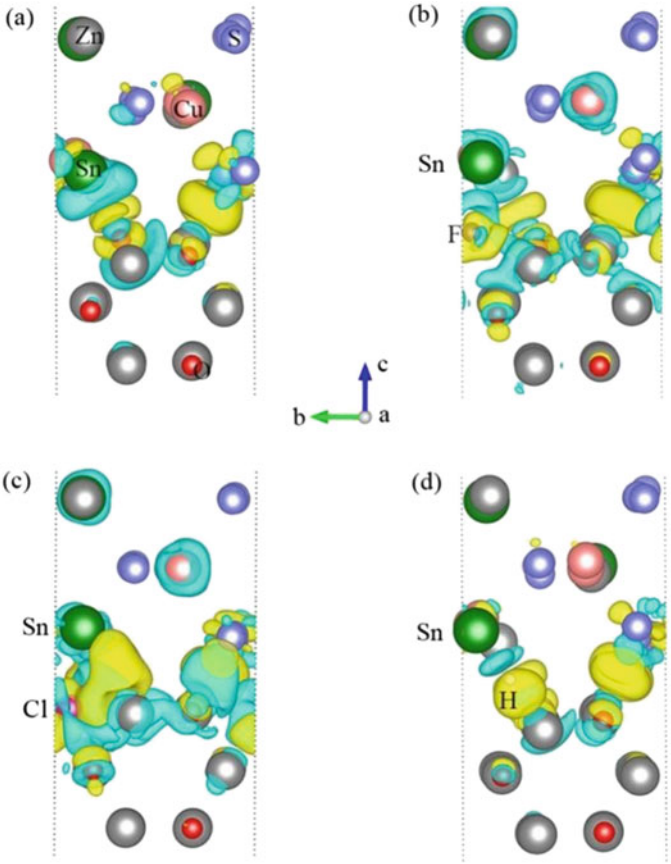

Fig. 2.23 The charge density difference for an interface without passivation (**a**) and with F (**b**), Cl (**c**), and H (**d**) passivation

Acknowledgments This work was financially supported by the National Natural Science Foundation of China (10964003, 11164014, and 11364025), the Petroleum Research Fund of the American Chemical Society (53827-UR10), and the Robert Welch Foundation (Departmental Grant, AC-0006).

The work in this chapter was performed in the Gansu Supercomputer Center. F.-L. Tang was financially supported by the Chinese Scholarship Council (201408625041). The authors thank the editors in allowing us to extend our previously published works as in the references.

References

1. W. Bao, M. Ichimura, Band offsets at the ZnO/Cu_2ZnSnS_4 interface based on the first principles calculation. Jpn. J. Appl. Phys. **52**, 061203 (2013)
2. P.E. Blöchl, O. Jepsen, O.K. Andersen, Improved tetrahedron method for Brillouin-zone integrations. Phys. Rev. B **49**, 16223 (1994)
3. I.V. Bodnar, I.N. Tsyrelchuk, I.A. Victorov, Preparation and analysis of the $CuAl_xIn_{1-x}Se_2$ solid solutions. J. Mater. Sci. Lett. **13**, 762–764 (1994)

4. Y.W. Cheng, F.L. Tang, H.T. Xue, et al., Bonding and electronic properties of the Cu_2ZnSnS_4/WZ-ZnO interface from first-principles calculations. J. Phys. D. Appl. Phys. **49**, 285107 (2016)
5. Y.W. Cheng, F.L. Tang, H.T. Xue, et al., First-principles study on electronic properties and lattice structures of WZ-ZnO/CdS interface. Mater. Sci. Semicond. Process. **45**, 9–16 (2016)
6. Y.W. Cheng, F.L. Tang, H.T. Xue, et al., Passivation for Cu_2ZnSnS_4/WZ-ZnO interface states: from the first principles calculations. Appl. Surf. Sci. **394**, 58–62 (2017)
7. J.W.D. Connolly, A.R. Williams, Density-functional theory applied to phase transformations in transition-metal alloys. Phys. Rev. B **27**, 5169 (1983)
8. Z. Derkaoui, Z. Kebbab, R. Miloua, et al., Theoretical study of optical characteristics of multilayer coatings ZnO/CdS/CdTe using first-principles calculations. Solid State Commun. **149**, 1231–1235 (2009)
9. Z.Y. Dong, Y.F. Li, B. Yao, et al., An experimental and first-principles study on band alignments at interfaces of Cu_2ZnSnS_4/CdS/ZnO heterojunctions. J. Phys. D. Appl. Phys. **47**, 075304 (2014)
10. M. Engelmann, B.E. McCandless, R.W. Birkmire, Formation and analysis of graded CuIn $(Se_{1-y}S_y)_2$ films. Thin Solid Films **387**, 14–17 (2001)
11. Y.N. Gornostyrev, M.I. Katsnelson, N.I. Medvedeva, et al., Peculiarities of defect structure and mechanical properties of iridium: results of ab initio electronic structure calculations. Phys. Rev. B **62**, 7802 (2000)
12. T. Hong, J.R. Smith, D.J. Srolovitz, Adhesion at a heterophase interface: first-principles study of Mo (001)/$MoSi_2$ (001). Interface Sci. **1**, 223–235 (1994)
13. G.Y. Huang, C.Y. Wang, J.T. Wang, Detailed check of the LDA+ U and GGA+ U corrected method for defect calculations in wurtzite ZnO. Comput. Phys. Commun. **183**, 1749–1752 (2012)
14. B. Huang, S. Chen, H.X. Deng, et al., Origin of reduced efficiency in Cu(In, Ga)Se_2 solar cells with high Ga concentration: alloy solubility versus intrinsic Defects. IEEE J. Photovoltaics **4**, 477–482 (2014)
15. G. Kresse, J. Furthmüller, Efficiency of ab-initio total energy calculations for metals and semiconductors using a plane-wave basis set. Comput. Mater. Sci. **6**, 15–50 (1996)
16. G. Kresse, J. Furthmüller, Efficient iterative schemes for ab initio total-energy calculations using a plane-wave basis set. Phys. Rev. B **54**, 11169 (1996)
17. G. Kresse, D. Joubert, From ultrasoft pseudopotentials to the projector augmented-wave method. Phys. Rev. B **59**, 1758 (1999)
18. Y. Kumagai, Y. Soda, F. Oba, et al., First-principles calculations of the phase diagrams and band gaps in $CuInSe_2$-$CuGaSe_2$ and $CuInSe_2$-$CuAlSe_2$ pseudobinary systems. Phys. Rev. B **85**, 033203 (2012)
19. X.K. Li, H.T. Xue, F.L. Tang, et al., First-principles calculation of sulfur-selenium segregation in $ZnSe_{1-x}S_x$: the role of lattice vibration. Mater. Sci. Semicond. Process. **39**, 96–102 (2015)
20. Y. Liu, M.R. Halfmoon, C.A. Rittenhouse, et al., Passivation effects of fluorine and hydrogen at the SiC-SiO_2 interface. Appl. Phys. Lett. **97**, 242111 (2010)
21. X. Liu, H. Cui, W. Li, et al., Improving Cu_2ZnSnS_4 (CZTS) solar cell performance by an ultrathin ZnO intermediate layer between CZTS absorber and Mo back contact. Phys. Status Solidi (RRL)-Rapid Res. Lett. **8**, 966–970 (2014)
22. H.X. Liu, F.L. Tang, H.T. Xue, et al., Lattice structures and electronic properties of WZ-$CuInS_2$/MoS_2 interface from first-principles calculations. Appl. Surf. Sci. **351**, 382–391 (2015)
23. C.D.R. Ludwig, T. Gruhn, C. Felser, et al., Indium-Gallium Segregation in $CuIn_xGa_{1-x}Se_2$: an ab initio-based Monte Carlo study. Phys. Rev. Lett. **105**, 025702 (2010)
24. F.D. Murnaghan, The compressibility of media under extreme pressures. Proc. Natl. Acad. Sci. **30**, 244–247 (1944)
25. J.P. Perdew, K. Burke, M. Ernzerhof, Generalized gradient approximation made simple. Phys. Rev. Lett. **77**, 3865 (1996)
26. J. Pohl, K. Albe, Thermodynamics and kinetics of the copper vacancy in $CuInSe_2$, $CuGaSe_2$, $CuInS_2$, and $CuGaS_2$ from screened-exchange hybrid density functional theory. J. Appl. Phys. **108**, 023509 (2010)
27. B. Puchala, A. Van der Ven, Thermodynamics of the Zr-O system from first-principles calculations. Phys. Rev. B **88**, 094108 (2013)

28. J. Sandino, E. Romero, J.S. Oyola, et al., Study of the Mo/$CuInS_2$/ZnS system by TEM. Sol. Energy Mater. Sol. Cells **95**, 2006–2009 (2011)
29. C.J. Sheppard, V. Alberts, Deposition of single-phase $CuIn(Se, S)_2$ thin films from the sulfurization of selenized CuIn alloys. J. Phys. D. Appl. Phys. **39**, 3760 (2006)
30. C.J. Sheppard, V. Alberts, W.J. Bekker, Deposition of $CuIn(Se, S)_2$ thin films by sulfurization of selenized Cu/In alloys. Phys. Status Solidi B **201**, 2234–2238 (2004)
31. C.J. Sheppard, V. Alberts, J.R. Botha, Structural and optical characterization of single-phase $CuIn(Se, S)_2$ thin films deposited using a two-step process. Phys. Status Solidi C **5**, 641–644 (2008)
32. F.L. Tang, Z.X. Zhu, H.T. Xue, et al., Optical properties of Al-doped $CuInSe_2$ from the first principle calculation. Physica B **407**, 4814–4818 (2012)
33. Y. Tani, K. Sato, H. Katayama-Yoshida, Materials design of spinodal nanodecomposition in $CuIn_{1-x}Ga_xSe_2$ for high-efficiency solar energy conversion. Appl. Phys. Express **3**, 101201 (2010)
34. T. Tinoco, C. Rincón, M. Quintero, et al., Phase diagram and optical energy gaps for $CuIn_yGa_{1-y}Se_2$ alloys. Phys. Status Solidi A **124**, 427–434 (1991)
35. T. Tinoco, J.P. Itié, A. Polian, et al., Combined x-ray absorption and x-ray diffraction studies of $CuGaS_2$, $CuGaSe_2$, $CuFeS_2$ and $CuFeSe_2$ under high pressure. J. Phys. IV **4**, 151–154 (1994)
36. S. Tomić, L. Bernasconi, B.G. Searle, et al., Electronic and optical structure of wurtzite $CuInS_2$. J. Phys. Chem. C **118**, 14478–14484 (2014)
37. A. Van De Walle, M. Asta, G. Ceder, The alloy theoretic automated toolkit: a user guide. Calphad **26**, 539–553 (2002)
38. W. Wang, K. Xiong, G. Lee, et al., Origin of HfO_2/GaAs interface states and interface passivation: a first-principles study. Appl. Surf. Sci. **256**, 6569–6573 (2010)
39. J.H. Werner, J. Mattheis, U. Rau, Efficiency limitations of polycrystalline thin film solar cells: case of $Cu(In, Ga)Se_2$. Thin Solid Films **480**, 399–409 (2005)
40. H.T. Xue, W.J. Lu, Z.X. Zhu, et al., Al-doped $CuInSe_2$: an ab initio study of structural and electronic properties of photovoltaic material. Adv. Mater. Res. **512**, 1543–1547 (2012)
41. H.T. Xue, F.L. Tang, W.J. Lu, et al., First-principles investigation of structural phase transitions and electronic properties of $CuGaSe_2$ up to 100GPa. Comput. Mater. Sci. **67**, 21–26 (2013)
42. H.T. Xue, W.J. Lu, F.L. Tang, et al., Phase diagram of the $CuInSe_2$-$CuGaSe_2$ pseudobinary system studied by combined *ab initio* density functional theory and thermodynamic calculation. J. Appl. Phys. **116**, 053512 (2014)
43. H.T. Xue, F.L. Tang, T. Gruhn, et al., Generalized stacking fault energies, cleavage energies, ionicity and brittleness of $Cu(Al/Ga/In)Se_2$ and $CuGa(S/Se/Te)_2$. Model. Simul. Mater. Sci. Eng. **22**, 035002 (2014)
44. H.T. Xue, F.L. Tang, X.K. Li, et al., Phase equilibrium of a $CuInSe_2$-$CuInS_2$ pseudobinary system studied by combined first-principles calculations and cluster expansion Monte Carlo simulations. Mater. Sci. Semicond. Process. **25**, 251–257 (2014)
45. H.T. Xue, F.L. Tang, F.Z. Zhang, et al., Effect of temperature on the distribution and inhomogeneity degree of Se-S atoms in $CuIn(Se_{1-x}S_x)_2$ alloys. J. Phys. D. Appl. Phys. **49**, 025101 (2016)
46. H.T. Xue, F.L. Tang, F.Z. Zhang, et al., Temperature effects on distribution and inhomogeneous degree of In-Ga atoms in $CuIn_{1-x}Ga_xSe_2$ alloys. Mater. Lett. **164**, 169–171 (2016)
47. Y. Yan, R. Noufi, K.M. Jones, et al., Chemical fluctuation-induced nanodomains in $Cu(In, Ga)Se_2$ films. Appl. Phys. Lett. **87**, 121904 (2005)
48. G. Yang, Y.F. Li, B. Yao, et al., Band alignments at the interface of Cu_2ZnSnS_4/ZnO heterojunction: an X-ray photoelectron spectroscopy and first-principles study. J. Alloys Compd. **628**, 293–297 (2015)
49. Y. Zhang, F.L. Tang, H.T. Xue, et al., Lattice structures and electronic properties of Mo/$MoSe_2$ interface from first-principles calculations. Phys. E. **66**, 342–349 (2015)
50. J.G. Zhou, D.M. Causon, C.G. Mingham, et al., The surface gradient method for the treatment of source terms in the shallow-water equations. J. Comput. Phys. **168**, 1–25 (2001)